APL Photonics

Dynamic metasurface lens based on MEMS technology

Cite as: APL Photonics 3, 021302 (2018); https://doi.org/10.1063/1.5018865
Submitted: 10 December 2017 • Accepted: 24 January 2018 • Published Online: 20 February 2018

Tapashree Roy, Shuyan Zhang, Il Woong Jung, et al.

Dynamic metasurface lens based on MEMS technology

Tapashree Roy,[1,2,a,b] Shuyan Zhang,[2,b] Il Woong Jung,[1] Mariano Troccoli,[3] Federico Capasso,[2] and Daniel Lopez[1]
[1]*Nanoscience and Technology Division, Argonne National Laboratory, Lemont, Illinois 60439, USA*
[2]*John A. Paulson School of Engineering and Applied Sciences, Harvard University, Cambridge, Massachusetts 02138, USA*
[3]*Evolution Photonics, Inc., Pasadena, California 91106, USA*

(Received 10 December 2017; accepted 24 January 2018; published online 20 February 2018)

In the recent years, metasurfaces, being flat and lightweight, have been designed to replace bulky optical components with various functions. We demonstrate a monolithic Micro-Electro-Mechanical System (MEMS) integrated with a metasurface-based flat lens that focuses light in the mid-infrared spectrum. A two-dimensional scanning MEMS platform controls the angle of the lens along two orthogonal axes by ±9°, thus enabling dynamic beam steering. The device could be used to compensate for off-axis incident light and thus correct for aberrations such as coma. We show that for low angular displacements, the integrated lens-on-MEMS system does not affect the mechanical performance of the MEMS actuators and preserves the focused beam profile as well as the measured full width at half maximum. We envision a new class of flat optical devices with active control provided by the combination of metasurfaces and MEMS for a wide range of applications, such as miniaturized MEMS-based microscope systems, LIDAR scanners, and projection systems.
https://doi.org/10.1063/1.5018865

I. INTRODUCTION

Recently, metasurface-based flat optical devices capable of shaping the wavefront of light have come to the forefront of ongoing scientific research.[1–3] Planar counterparts of conventional bulky optical devices like lenses,[4–6] beam deflectors,[7,8] holograms,[9] polarimeters,[10] and so on have been experimentally demonstrated. These devices use sub-wavelength dimension metallic and/or dielectric phase shifting optical elements arranged on a two-dimensional plane, "metasurface," mimicking the phase profile of the conventional bulk optical device. Such metasurface-based flat devices represent a new class of optical components that are compact and lightweight. However, most of these nanostructured devices are static, which limits the functions that can be achieved.

In this paper, we introduce the concept of dynamically controlling these metasurfaces by integrating them onto Micro-Electro-Mechanical Systems (MEMS). These MEMS have the unique advantages of high-speed movement, excellent optical quality, wavelength and polarization independence, and low optical loss.[11] We present a prototype consisting of a MEMS-controlled reflective metasurface lens that focuses in the mid-infrared spectrum. The preferred MEMS device is an electrostatically controlled 2D scanner micro-mirror because it is a key element used in many applications such as LIDAR laser scanners,[12] optical communications,[13,14] and bio-imaging.[15–18] Technologies like these will greatly benefit from a dynamically controlled metasurface-based lens because it will facilitate the removal of bulky optical components in the system while allowing unique functions such

[a]Present address: Applied Materials, Inc., Mumbai 400076, India.
[b]T. Roy and S. Zhang contributed equally to this work.

as the predetermined shaping of light beams. When electrostatically actuated, the MEMS platform controls the angle of the lens along two orthogonal axes allowing scanning of the flat lens focal spot by about ±9° in each direction.

II. SAMPLE DESIGN AND FABRICATION

We design a plasmonic lens producing a line focus, like a cylindrical lens, when illuminated with monochromatic mid-infrared light of wavelength $\lambda = 4.6\ \mu$m. As the design unit cells, we choose polarization independent, sub-wavelength-sized, 50 nm-thick gold resonators in the shape of a disc [Fig. 1(a)]. The resonators sit on a 400 nm-thick silicon dioxide layer deposited on a 200 nm-thick continuous gold film. This structure has been used to improve the focusing efficiency in reflection.[19,20] By changing the radius of the disc, the phase of the reflected light changes [Fig. 1(b)]. To construct a planar lens, we spatially distribute the discs with varying radii to realize the hyperbolic phase profile. Figure 1(c) shows a schematic of the reflective metasurface lens when a collimated Gaussian beam is incident at an angle θ on the lens and is focused at a distance f along the normal axis to the lens surface. This configuration proves the flexibility of our design technique: by using the metasurface itself to spatially separate the incident and reflected beams, we avoid the need for a beam splitter, resulting already in a reduction in the number of bulk optical components that are conventionally used in optical systems.

The equation of the phase profile used to design the metasurface lens is

$$\varphi(x) = \frac{2\pi}{\lambda}\left(f - \sqrt{x^2 + f^2} - x \cdot \sin\theta\right),$$

where λ is the wavelength, f is the focal length, and x is the position of the phase shifting elements in the lens. The lens functions as a cylindrical lens, i.e., one-dimensional focusing, so the phase profile is only a function of x.[19] One improvement from the previous literature[21] is that the overall packing density of the subwavelength resonators is increased by arranging them with constant edge-edge

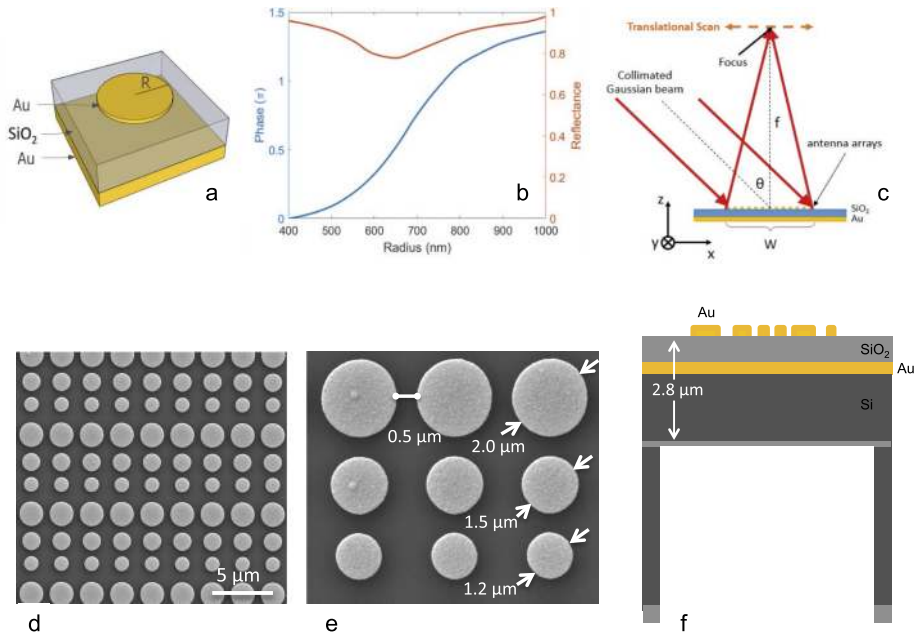

FIG. 1. Design and fabrication of the metasurface lens: (a) A unit cell consisting of a 50 nm-thick gold disc on 400 nm-thick silicon dioxide substrate with a 200 nm-thick gold backplane. (b) Simulated values of reflectance and phase for varying sizes of gold discs. (c) Schematic representation of focusing characteristics of the reflective metasurface lens for tilted illumination. [(d) and (e)] Scanning electron microscope images of the fabricated lens. (f) Schematic cross section of the different constituting layers of the membrane-supported flat lens.

distance. An increase in the packing density means that the sampling rate of the phase profile of the metasurface lens is increased leading to smaller phase errors introduced by digitizing the phase profile and, hence, an improvement in the metasurface performance. The metasurface lens demonstrated here is designed on a square layout with each side measuring W = 0.8 mm to focus light incident at an angle of θ = 45° to the lens surface at a distance f = 5 mm away.

The metasurface lens is fabricated using standard photolithography techniques on a silicon-on-insulator (SOI) wafer with a 2 μm-thick top device layer, a 200 nm buried-oxide layer, and a 600 μm-thick handle layer. SEM images of the reflective lens are shown in Figs. 1(d) and 1(e). The detailed process flow for fabricating the lens is described in S1 of the supplementary material. Following the lens fabrication, the handle layer is removed using a dry-etch process based on xenon-difluoride, resulting in a reflective flat lens standing on top of a 2.8 μm-thick membrane [Fig. 1(f)]. For the next stage of fabrication, we use a focused ion beam (FIB) tool integrated with an Omniprobe micromanipulator needle to integrate the flat lens onto a 2D MEMS scanner. Figure 2(a) depicts the steps of the process. We trace the focused ions around the periphery of the lens to cut out most of the structure, except a small portion. Here we weld the needle-tip of the micromanipulator by depositing platinum. The remaining structure is subsequently released; the membrane is free from the surrounding solid substrate and is held only by the micromanipulator needle. We move the membrane out of the substrate and on to the MEMS platform by controlling the micromanipulator arm. After the lens is placed and aligned with the central platform of the MEMS, it is *glued* by depositing platinum in small patches. Finally the needle is cut away by milling with focused ion beam.[22] This practical technique allows for fusion welding of the flat lens to the MEMS device without the need for extra materials. Moreover, it enables the integration of hybrid structures fabricated with processes having different critical dimensions and structural materials (see S2 of the supplementary material).

An optical image of the 2D MEMS scanner with the integrated flat lens is shown in Fig. 2(b). The scanner is gimbaled for achieving biaxial degrees-of-freedom and is actuated by electrostatic vertical comb drives.[11] Vertical comb-drives consist of stationary plates interspersed with the rotating ones. When a potential difference is applied between these plates, the moving elements are pulled downward causing a rotation around a particular axis. Simple single-layer straight beams are used for torsional flexures on both inner and outer axes to give a 2-D rotational degree-of-freedom. The micromirror is electrostatically rotated about the inner axis using the vertical comb drives mounted on the gimbal frame.[15] The gimbal frame rotates about the outer axis using the vertical comb drives mounted on its frame and substrate. For the devices reported here, the typical maximum angular displacement is close to ±9° and the resonance frequency is of the order of 1 kHz about each torsional axis. The mirror dimensions are 1 mm × 1 mm with a thickness of 10 μm. Although thicker device layers are desired for better flatness of mirrors and frame under dynamic deformation, they are also more difficult to fabricate due to the required high aspect-ratio fabrication process and alignment issues. Simulations showed that 10 μm-thick layers provide sufficiently large stable

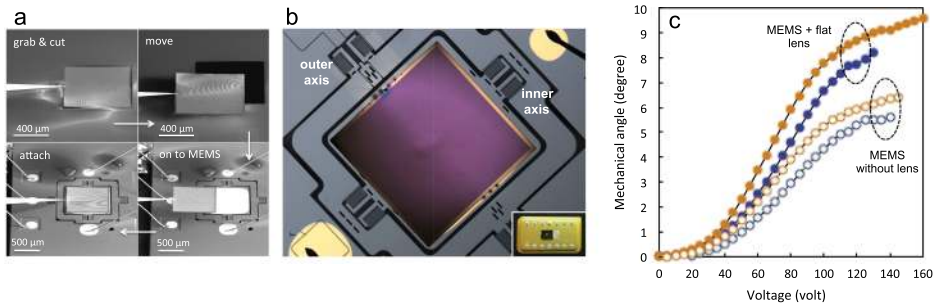

FIG. 2. Integration of the flat lens onto MEMS: (a) Stages of integration of the metasurface-based flat lens with an external 2D MEMS platform. (b) Optical microscope image of a MEMS scanner with a flat lens on top. The two rotational axes of the scanner are indicated. The inset shows the device mounted on a dual in-line package ready for electrostatic actuation. (c) Angular displacement of the MEMS scanner with and without the metasurface-based lens. The orange circles represent the angular displacement when the inner axis is actuated, while the blue circles show the response when the outer axis is activated.

deflection range with minimal adverse effect on the performance of the device caused by the dynamic deformations of the rotating MEMS platform.[11] To characterize the mechanical response of the flat lens-on-MEMS assembly, the device is mounted on a dual in-line package and electrostatically actuated to independently control either the inner or the outer axes, as shown in Fig. 2(b). Details of the MEMS platform working principle and voltage connections are given in S3 of the supplementary material. Figure 2(c) summarizes the mechanical response of the MEMS scanner when a voltage is applied across each rotational axis. As the applied voltage is increased, the MEMS mirror starts rotating until a saturating region is reached, beyond which the comb drives cannot be moved further. We perform this experiment under an optical profilometer, capturing an image of the MEMS surface for each applied voltage. The rotation angle of the MEMS mirror is calculated with respect to a rigid peripheral structure. The measurements are taken for bare MEMS, i.e., before the metasurface lens has been integrated, and for the same device after it has been loaded with the metasurface lens. As shown in Fig. 2(c), even after the addition of the metasurface lens on top of the MEMS, the functional dependence of the MEMS mirror remains the same. The increased angular dependence of the loaded MEMS is a consequence of using vertical comb drives for torsional actuation of the device. The incorporation of the flat lens onto the micro-mirror reduces the static gap between vertical combs resulting in a much efficient actuation and, thus, a larger angular deflection.

III. OPTICAL CHARACTERIZATION

The focusing characteristic of the flat lens is simulated by using the Finite Difference Time Domain (FDTD) method (Lumerical, Inc.). Only one row of nano-disc antennas along the x-direction where the phase profile of the cylindrical lens has been imposed is simulated, while Bloch boundary conditions are applied along the y-directions. Figure 3(a) is the calculated distribution of the electric field intensity ($|E|^2$) near the focal region in the x-z plane. The focal length is determined by the z value of the highest intensity point, which is indicated by the white dashed line at $z = f = 5$ mm. The focusing efficiency is estimated to be 83%, which is calculated from the beam intensity at the focal region normalized to the source power. Figure 3(b) shows the beam profile at the focal region across the dashed line in Fig. 3(a). The simulated discrete data points (blue circles) are fitted with a Gaussian curve (red line) to determine the full width at half maximum (FWHM) of the focal beam, which is 22.8 μm. This is only slightly bigger than the diffraction-limited value (21.6 μm), possibly due to the discrete phase approximation of the ideal 0–2π variation.

For the experimental characterization, we use a continuous-wave Fabry-Pérot quantum cascade laser (QCL) (AdTech Optics) emitting at $\lambda = 4.6$ μm. The laser is mounted so that its output beam is s-polarized (electric field of the light is first sent through a pinhole before reaching the detector). Because of the small focused beam size, another dual-lens system is placed before the detector to expand the focused beam by a factor of 2.5 (see S4 of the supplementary material). The signal-to-noise ratio is increased by modulating the intensity of the QCL with a small sinusoidal current superimposed on the direct current (Wavelength Electronics QCL1500) and demodulating the detected signal with a lock-in amplifier (AMETEK Advanced Measurement Technology).

The focus is characterized experimentally by translational scans. The data are taken at the center of the focal line, i.e., $y = 0$. The average standard deviation of repeated measurements is 0.2%. The detector is scanned across the focus in 2 μm steps, which is smaller than the pinhole diameter (10 μm). So, the raw data are de-convoluted to retrieve the original beam profiles. Figure 3(c) shows the measurement results of the metasurface lens on a solid substrate. The FWHM is 26.2 μm, which is close to the simulated value. The difference is possibly due to fabrication errors and the M^2 factor of the QCL not being 1 ($M^2 = 1.2$). The side lobes in Fig. 3(b) are not observed because of the increased FWHM in Fig. 3(c).

The optical focusing performance of the metasurface lens integrated with the MEMS is experimentally characterized using the same setup as described above. The angle of the incident light is at 45° to the unactuated MEMS scanner. The profile of the reflected focal line is measured for three positions of the MEMS platform: actuating voltages of 0 V (unactuated), 40 V, and 60 V are applied across the outer axis such that the lens tilts by 0°, 1°, and 2.5°, respectively [Figs. 3(d)–3(f)]. The measured FWHM of the focal lines for the three tilted positions of the lens are shown in

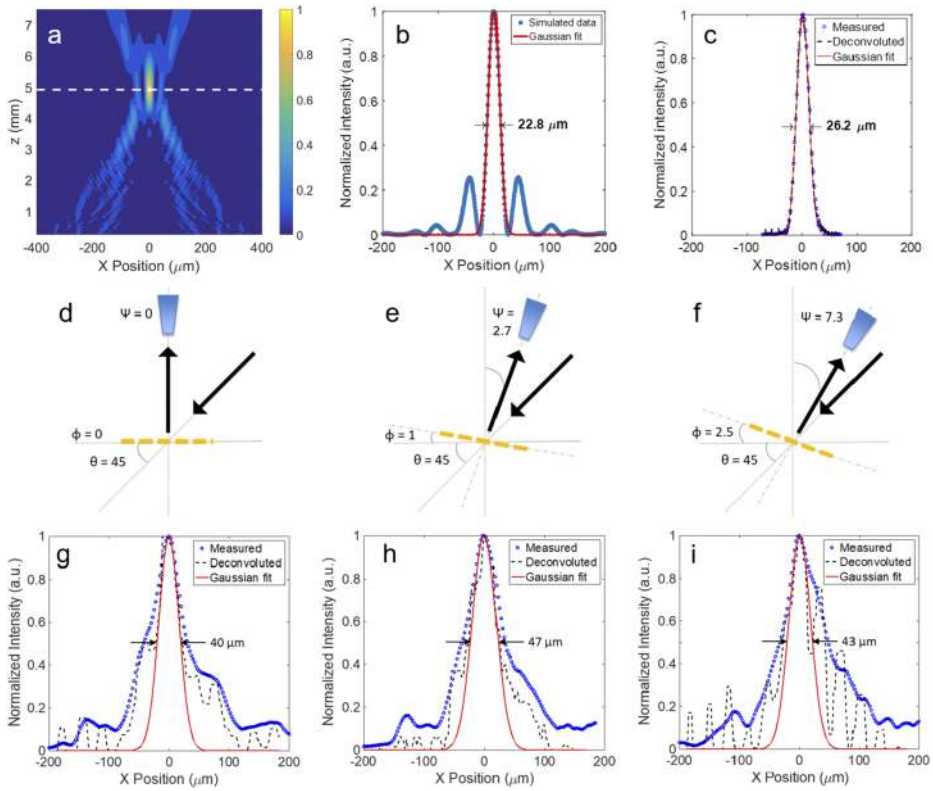

FIG. 3. (a) Simulation: distribution of the intensity (normalized $|E|^2$) of the reflected beam in the x-z plane at y = 0. The lens is centered at x = 0 and the size of the lens is from −0.4 mm to 0.4 mm consisting of 374 antennas. The white dashed line indicates the focal length. (b) Simulation: line scan of the focused beam profile at y = 0 and z = f = 5 mm along the white dashed line. (c) Experiment: translational scan of the reflected beam intensity (normalized $|E|^2$) measured at the center of the focal line. [(d)–(f)] Schematic of the three experimental configurations: the MEMS scanner is actuated to move the lens by 0°, 1°, and 2.5°, respectively, while the angle of the incident illumination remains unchanged. To align with the peak of the reflected signal, the position of the detector needs to be at 0°, 2.7°, and 7.3° respectively. [(g)–(i)] Optical profile at the focal line of the reflected beam when the actuated lens-on-MEMS device is rotated by 0°, 1°, and 2.5°, respectively. Experimentally measured translation scan for each of the three configurations. The FWHMs calculated from the Gaussian fits are comparable though the asymmetry of the central peak changes with the tilting of the platform.

Figs. 3(g)–3(i), respectively. For each position of the lens, the detector is rotated to align with the peak intensity of the reflected light. To measure the beam profile, a translational scan is performed across the rotated focal line position with a 30 μm pinhole in 5 μm steps. For the designed 0° position of the MEMS platform, when compared to the lens on the solid substrate [Fig. 3(c)], we observe an increase in FWHM. This is attributed to the non-flatness of the lens when released from the solid substrate. Another factor is that when the device plane is rotated, the incident angle is no longer the same as the designed angle (45°), and hence it introduces phase errors affecting the focusing performance. However, tilting the MEMS integrated lens up to 2.5° preserves the focused beam profile in general as well as the measured FWHM. The simulation results and analysis are further summarized in Fig. S5 of the supplementary material. For dynamic coma correction, one would rotate the device plane according to the change of incident angle so as to keep the incident angle constant.

In order to quantify the effect of the surface curvature on the otherwise designed *flat* lens performance, we measure the curvature of the lens-on-MEMS assembly using an optical profilometer and simulate the performance of a cylindrical lens on top of a substrate having the same curvature (see S6 of the supplementary material for details). The results are shown in Fig. 4. When supported by the curved substrate, the focal length of the lens increases to 8.9 mm compared to the designed value of 5 mm, and the reflected beam path is at 0.5° compared to the designed value of 0°. The FWHM becomes wider, 41.7 μm compared to 22.8 μm as on a solid substrate, which is in reasonable agreement with the results reported in Figs. 3(g)–3(i).

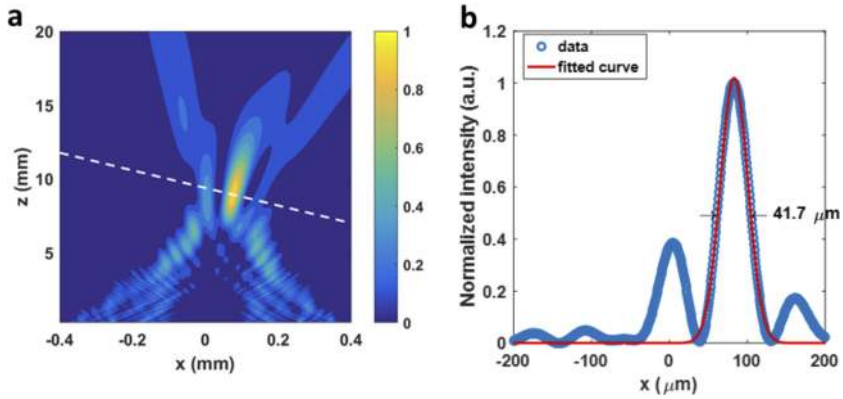

FIG. 4. (a) Distribution of the intensity (normalized $|E|^2$) of the reflected beam in the x-z plane at y = 0 with a curved substrate. The white dashed line is perpendicular to the reflected beam path. (b) Simulated line scan of the focused beam profile along the white dashed line.

IV. CONCLUSION

In summary, we have presented a MEMS-integrated metasurface lens. The device can be electrically controlled to vary the 2D angular rotation of a flat lens and hence the position of the focal spot by several degrees. This proof-of-concept integration of metasurface-based flat lenses with 2D MEMS scanners can be extended to the visible and other parts of the electromagnetic spectrum implying the potential for application across wider fields, such as MEMS-based microscope systems, holographic and projection imaging, LIDAR scanners, laser printing, and so on. Dense integration of thousands of individually controlled lens-on-MEMS devices onto a single silicon chip would lead to the creation of a new type of reconfigurable fast digital Spatial Light Modulator[23] that would allow an unprecedented degree of control and manipulation of the optical field. Moreover, each metasurface element could be made reconfigurable by integrating with more complicated MEMS designs, such as recent demonstrations involving MEMS cantilevers as unit cells.[24–26]

SUPPLEMENTARY MATERIAL

See supplementary material for more details on the fabrication and characterization of the MEMS devices and metasurfaces described in this work.

ACKNOWLEDGMENTS

We acknowledge Tobias Mansuripur for the valuable advice on the experiments and Alan She for helpful discussions. We acknowledge the funding support from Air Force Office of Scientific Research (AFOSR) (No. MURI: FA9550-12-1-0389). Shuyan Zhang acknowledges the funding support from National Science Scholarship from A∗STAR, Singapore. This work was performed in part at the Center for Nanoscale Systems (CNS), a member of the National Nanotechnology Infrastructure Network (NNIN), which is supported by the National Science Foundation under NSF Award No. ECS-0335765. CNS is part of Harvard University. Use of the Center for Nanoscale Materials was supported by the U.S. Department of Energy, Office of Science, Office of Basic Energy Sciences, under Contract No. DE-AC02-06CH11357.

[1] N. Yu and F. Capasso, "Flat optics with designer metasurfaces," Nat. Mater. **13**, 139–150 (2014).
[2] N. Yu *et al.*, "Light propagation with phase discontinuities: Generalized laws of reflection and refraction," Science **334**, 333–337 (2011).
[3] M. Decker *et al.*, "High-efficiency dielectric Huygens' surfaces," Adv. Opt. Mater. **3**, 813–820 (2015).
[4] T. Roy, E. T. F. Rogers, and N. I. Zheludev, "Sub-wavelength focusing meta-lens," Opt. Express **21**, 7577 (2013).
[5] F. Aieta *et al.*, "Aberration-free ultrathin flat lenses and axicons at telecom wavelengths based on plasmonic metasurfaces," Nano Lett. **12**, 4932–4936 (2012).
[6] M. Khorasaninejad *et al.*, "Metalenses at visible wavelengths: Diffraction-limited focusing and subwavelength resolution imaging," Science **352**, 1190–1194 (2016).

[7] T. Roy, A. E. Nikolaenko, and E. T. F. Rogers, "A meta-diffraction-grating for visible light," J. Opt. **15**, 085101 (2013).
[8] N. Yu *et al.*, "Flat optics: Controlling wavefronts with optical antenna metasurfaces," IEEE J. Sel. Top. Quantum Electron. **19**, 4700423 (2013).
[9] X. Ni, A. V. Kildishev, and V. M. Shalaev, "Metasurface holograms for visible light," Nat. Commun. **4**, 2807 (2013).
[10] J. P. B. Mueller, K. Leosson, and F. Capasso, "Ultracompact metasurface in-line polarimeter," Optica **3**, 42–47 (2016).
[11] O. Solgaard, *Photonic Microsystems: Micro and Nanotechnology Applied to Optical Devices and Systems* (Springer Verlag, 2008).
[12] B. Schwarz, "LIDAR: Mapping the world in 3D," Nat. Photonics **4**, 429–430 (2010).
[13] M. C. Wu, O. Solgaard, and J. E. Ford, "Optical MEMS for lightwave communication," J. Lightwave Technol. **24**, 4433–4454 (2006).
[14] V. Aksyuk*et al.*, "Optical MEMS design for telecommunications applications," in Proceedings of the Solid-State Sensor, Actuator and Microsystems Workshop, Hilton Head Island, South Carolina, 2002.
[15] I. W. Jung *et al.*, "2-D MEMS scanner for handheld multispectral confocal microscopes," in *2012 International Conference on Optical MEMS and Nanophotonics* (IEEE, 2012), pp. 238–239.
[16] S. Rattanavarin *et al.*, "MEMS based multispectral confocal probe," in *2013 Transducers & Eurosensors XXVII: The 17th International Conference on Solid-State Sensors, Actuators and Microsystems (TRANSDUCERS & EUROSENSORS XXVII)* (IEEE, 2013), pp. 2173–2176.
[17] C. Yin *et al.*, "Miniature *in vivo* MEMS-based line-scanned dual-axis confocal microscope for point-of-care pathology," Biomed. Opt. Express **7**, 251–263 (2016).
[18] W. Jung *et al.*, "Miniaturized probe using 2 axis MEMS scanner for endoscopic multiphoton excitation microscopy," Proc. SPIE **6851**, 68510D (2008).
[19] S. Zhang *et al.*, "High efficiency near diffraction-limited mid-infrared flat lenses based on metasurface reflectarrays," Opt. Express **24**, 18024–18034 (2016).
[20] S. Sun *et al.*, "High-efficiency broadband anomalous reflection by gradient meta-surfaces," Nano Lett. **12**, 6223–6229 (2012).
[21] M. Khorasaninejad and F. Capasso, "Metalenses: Versatile multifunctional photonic components," Science **358**, eaam8100 (2017).
[22] B. Park, I. W. Jung, J. Provine, O. Solgaard, and R. T. Howe, "Highly sensitive monolithic silicon photonic crystal fiber tip sensor for simultaneous measurement of refractive index and temperature," J. Lightwave Technol. **29**(9), 1367–1374 (2011).
[23] B. Dennis *et al.*, "Compact nanomechanical plasmonic phase modulators," Nat. Photonics **9**, 267–273 (2016).
[24] W. M. Zhu *et al.*, "Microelectromechanical Maltese-cross metamaterial with tunable terahertz anisotropy," Nat. Commun. **3**, 1274 (2012).
[25] L. Cong *et al.*, "Active multifunctional microelectromechanical system metadevices: Applications in polarization control, wavefront deflection, and holograms," Adv. Opt. Mater. **5**, 1600716 (2017).
[26] L. Cong, P. Pitchappa, C. Lee, and R. Singh, "Active phase transition via loss engineering in a terahertz MEMS metamaterial," Adv. Mater. **29**, 1700733 (2017).